C. R. Chimie 22 (2019) 667–677

Contents lists available at ScienceDirect

Comptes Rendus Chimie

www.sciencedirect.com

Full paper / Mémoire

Effect of ion (Ag^{+}, N^{3-}) doping on the photocatalytic activity of the Ruddlesden–Popper-type layered perovskite $K_2Nd_2Ti_3O_{10}$

Ramaswamy Kadari [a], Gundeboina Ravi [b], Perala Venkataswamy [b], Radha Velchuri [c], Nagegownivari Ramachandra Munirathnam [a, **], Muga Vithal [b, *]

[a] Centre for Materials for Electronics Technology (CMET), Cherlapally, HCL (PO), Hyderabad, 500 051, India
[b] Department of Chemistry, University College of Science, Osmania University, Hyderabad, 500 007, India
[c] Mahatma Jyothibha Phule Telangana Backward Class Welfare Residential Degree College for Women, Wargal, 502 279, India

ARTICLE INFO

Article history:
Received 14 August 2019
Accepted 8 October 2019
Available online 15 November 2019

Keywords:
Layered perovskites
X-ray diffraction
FT-IR
TEM
Bandgap energy
Photocatalysis

ABSTRACT

In recent years, metal–nonmetal codoping has become a promising approach that can be used for effective tailoring of the structure–activity properties of semiconductors in photocatalysis. In the present study, N-doped $K_2Nd_2Ti_3O_{10}$ (KNdTON), Ag-doped $K_2Nd_2Ti_3O_{10}$ (AgNdTO), as well as N and Ag codoped $K_2Nd_2Ti_3O_{10}$ (AgNdTON) photocatalysts were successfully synthesized by solid-state and ion-exchange methods, using the pre-prepared $K_2Nd_2Ti_3O_{10}$ (KNdTO). The parent $K_2Nd_2Ti_3O_{10}$ catalyst was synthesized using a facile gel-burning method. The prepared materials are characterized by different techniques such as powder X-ray diffraction (XRD), thermogravimetric (TG) analysis, scanning electron microscopy–energy dispersive X-ray (SEM–EDX) spectroscopy, transmission electron microscopy (TEM), high- resolution-TEM (HR–TEM), oxygen–nitrogen–hydrogen (O–N–H) analysis, inductively coupled plasma-optical emission spectroscopy (ICP-OES), Fourier transform-infrared spectroscopy (FT-IR), and diffuse reflectance UV–visible spectroscopy (UV–vis DRS). The photocatalytic activity of the obtained catalysts was investigated by studying the degradation of two different pollutants viz., methylene blue (MB) and methyl violet (MV) under visible light irradiation. The shift in the XRD peaks and absorption edges confirms the incorporation of guest ions into the lattice of KNdTO. The photocatalytic degradation of MB and MV is found to be significantly improved via metal mono-doping and codoping. In particular, AgNdTON showed a remarkable increase in photodegradation compared to KNdTON, AgNdTO, and KNdTO. Such an improved photocatalytic activity of AgNdTON is due to the extended visible light absorption and the lower bandgap energy. Furthermore, AgNdTON demonstrated reasonable photocatalytic activity for the MV degradation up to five cycles.

1. Introduction

Because of technological advances, researchers have been facing problems such as the depletion of conventional energy sources and environmental pollution [1]. The development of alternative energy sources and waste-free

* Corresponding author.
** Corresponding author.
E-mail addresses: rathnam1960@gmail.com (N.R. Munirathnam), muga_vithal@rediffmail.com (M. Vithal).

https://doi.org/10.1016/j.crci.2019.10.004
1631-0748/

technologies are approaches to overcome these challenges. Semiconductor-mediated photocatalysis is one of such technologies and has gained immense interest owing to its applications in renewable energy and environmental remediation. The studies on the different types of semiconductor materials to produce clean hydrogen energy and for the degradation of environmental pollutants by utilizing solar energy have been continuing since the last two decades [2–8].

The investigations on layered perovskite-type oxides with a Ruddlesden–Popper (RP) phase structure have been appealing the researchers because of their ionic conductivity, superconductivity, catalytic, photocatalytic activity, structural specifics, and some unique properties, in particular, the ability to intercalate molecules into their interlayer space, ion-exchange reactions, and exfoliation to nanosheets [9–12]. The general formulae of RP phases is M_2 $[A_{n-1}B_nO_{3n+1}]$, with n = 1,2,3, etc. The structure of $M_2A_2B_3O_{10}$, one type of RP phase with $n = 3$, is characterized by the pristine perovskite blocks intercalated by rock salt layers, in which larger cations (M^+) are located, as shown in Fig. 1 [13–15].

The interlayer cations can be exchangeable with other cations. Gopala Krishnan et al. have prepared layered perovskite-type oxides $A_2Ln_2Ti_3O_{10}$ (A = K or Rb; Ln = La or rare-earth element) and studied the exchange of interlayer alkali-metal ions with protons as well as other alkali-metal ions under mild conditions [13]. Richard et al. have synthesized $A_2Nd_2Ti_3O_{10}$ (A = Na, K) using a solid-state reaction (SSR) method and investigated the thermal stability of parent and acid exchanged materials [14]. The composition, $K_2Nd_2Ti_3O_{10}$, is prepared using a flux method, and its crystal structure is reported [15]. Stearic acid assisted sol–gel method is employed to prepare $K_2Ln_2Ti_3O_{10}$ (Ln = La, Nd, Sm, Gd, and Dy) and their photocatalytic properties are investigated [16,17]. Layered perovskite-type oxides $A_2Ln_2Ti_3O_{10}$ (A = Li, Na, K; Ln = La, Nd) are prepared, and their (i) intercalation, (ii) optical properties, and (iii) photocatalytic properties are investigated [18]. Utkina et al. demonstrated the instability of $K_2Nd_2Ti_3O_{10}$ to hydration and protonation reactions in an aqueous medium with and without a humid atmosphere [19,20].

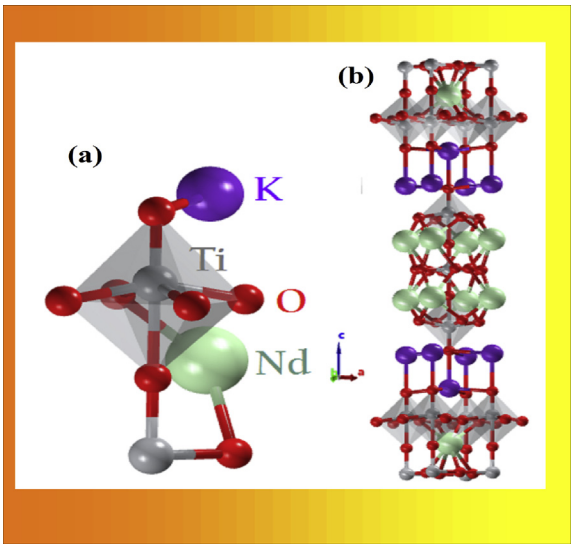

Fig. 1. Structure of Ruddlesden–Popper type layered perovskite $K_2Nd_2Ti_3O_{10}$.

Codoping with cation and anions is known to create intermediate electronic bands in the gap region, leading to substantial reduction in the bandgap energy. Such a modification of bandgap energy is beneficial in obtaining (i) Li-ion batteries with better efficiency [21], (ii) solar cells with higher efficiency [22], (iii) catalysts with enhanced oxygen evolution reaction in water splitting [23], and (iv) semiconductors with much improved photocatalytic activity [24]. For example, Sun et al. improved the solar water splitting activity of Ruddlesden–Popper type compound Sr_2TiO_4 by codoping with La^{3+}/N^{3-} ions [25]. Vinod et al. reported the enhancement of the photocatalytic degradation of RhB of $K_2La_2Ti_3O_{10}$ with the codoping of Sn^{2+}/N^{3-} ions [26]. Jeyalakshmi et al. reported the improvement of CO_2 photo-reduction on $Sr_3Ti_2O_7$ codoped with N, S, and Fe [27]. The codoping strategy is used in the present investigation to dope the $K_2Nd_2Ti_3O_{10}$ lattice with Ag^+ and N^{3-} ions. To the best of our knowledge, the photocatalytic activity studies of Ag^+ and N^{3-} codoped $K_2Nd_2Ti_3O_{10}$ are not reported. The present work deals with the preparation, characterization, and photocatalytic activity of parent $K_2Nd_2Ti_3O_{10}$ and doping/codoping of Ag^+ and N^{3-} $K_2Nd_2Ti_3O_{10}$ lattice.

2. Experimental section

2.1. Preparation of $K_2Nd_2Ti_3O_{10}$

Parent $K_2Nd_2Ti_3O_{10}$ (hereafter abbreviated as KNdTO) was prepared using an ethylene glycol assisted gel-burning method. Potassium nitrate (Merck), neodymium nitrate (Sigma Aldrich; neodymium oxide was dissolved in nitric acid (Merck) to obtain neodymium nitrate solution), titanium powder (Sigma Aldrich), ammonia (SDFCL), and hydrogen peroxide (Merck) were used as the starting materials. In a typical synthetic process, the stoichiometric amount of titanium powder was dissolved in 1:3 mixture of ammonia and hydrogen peroxide (10 mL of NH_3 and 30 mL of 30% H_2O_2). To this solution, aqueous potassium nitrate solution and neodymium nitrate solutions were added under constant stirring. Subsequently, citric acid (CA) was added to this solution such that the mole ratio of metal ions to CA is 1:2. Then, the pH of the solution was adjusted to about ~7 by adding a dilute ammonia solution. The resultant solution was thoroughly stirred for several hours at room temperature followed by slow evaporation until a viscous liquid was obtained. At this stage, ethylene glycol (EG) was added in the molar ratio of metal ions to EG of 1:2.4, and then it was heated at 150 °C for 4–5 h. The temperature was increased to 180–200 °C at the commencement of solidification. The obtained porous solid mass was crushed in an agate mortar and heated at 400 °C in small amounts in an electric burner to remove the organic matter. The obtained ash color solid was calcined at 900 °C for 12 h in a muffle furnace at atmospheric pressure in the air. The color of the resultant solid was dark ash.

2.2. Preparation of N-doped KNdTO

The solid-state method was used to prepare N-doped KNdTO. Urea was used as the source of nitrogen. The N-doped KNdTO was obtained by heating a thoroughly ground 1:2 weight ratio mixture of KNdTO and urea at 400 °C for 2 h in a muffle furnace in air. The resultant material was washed with distilled water to remove unreacted urea and dried at 60 °C. The obtained material was light brown in color and designated as KNdTON.

2.3. Ag-doped KNdTO and KNdTON

An ion-exchange method was adopted to prepare Ag-doped KNdTO and KNdTON. Silver nitrate (SDFCL) was used as received. Typically, KNdTO and KNdTON powders (1 g each) were added to 0.1 M $AgNO_3$ aqueous solution separately at room temperature under constant stirring. To ensure the maximum percentage of ion-exchange, the stirring was continued overnight, and the obtained products were washed several times with distilled water and dried in air at 60 °C. The AgNdTO and AgNdTON samples were light green and dark green in color, respectively.

2.4. Characterization of catalysts

The powder XRD patterns of as-prepared materials were recorded using a Rigaku miniflex X-ray diffractometer with Cu Kα radiation (1.54 Å). Diffractograms were recorded in the 2θ range of 4°–80° with a scan rate of 10° min^{-1}. The TG profiles are obtained using a PerkinElmer TGA 4000 instrument. The powder samples were heated from 35 to 1000 °C at 10 °C min^{-1} under flow of N_2. The SEM–EDX measurements were obtained from a HITACHI SU-1500 variable pressure scanning electron microscope (VP-SEM). The sample powder was deposited on carbon tape placed on a stub. TEM and HR–TEM images were obtained using a JEOL 2010 instrument operating at 200 kV. Before the TEM measurements, the samples were dispersed in ethanol for 15 min using the ultrasonic bath and then deposited onto a polymer-coated copper grid. The weight percentage of constituent elements in the samples was estimated from ICP-OES, Agilent 725 series. The O–N–H analysis was carried out using a LECO O–N–H 836 analyzer. FT-IR spectra were recorded using a Shimadzu spectrometer in the range 4000–250 cm^{-1}. The material was mixed with KBr and pressed into a thin pellet. UV–vis DRS spectra were acquired on a JASCO V650 UV/vis spectrophotometer in the range 200–800 nm. $BaSO_4$ was used as a reference.

2.5. Photocatalytic degradation experiments

The photocatalytic activity studies of KNdTO, AgNdTO, KNdTON, and AgNdTON were monitored through the photodegradation of MB and MV under visible light irradiation using a HEBER visible annular type photoreactor. A 300-W tungsten lamp (wavelength range: 380–840 nm) was used as a light source. A glass tube (~35 cm long and ~2.5 cm diameter) was used for the dye solution. The distance between the light source and dye solution was about ~7–8 cm. In a typical process, 60 mL of aqueous MB (or MV) solution with an initial concentration of 1×10^{-5} M and 60 mg of catalyst was taken in a cylindrical-shaped glass reactor at room temperature with continuous air bubbling to ensure a constant source of dissolved oxygen. The suspension was stirred in the dark for 60 min to establish adsorption–desorption equilibrium before irradiation. During the irradiation process, at regular 30 min intervals, about 2–3 mL of the solution was collected and centrifuged to remove the catalyst particles. The changes in the concentration of MB and MV were obtained by recording the absorbance at 664 and 580 nm, respectively, using a Jasco V650 UV–vis spectrophotometer. The degradation amount of dyes was calculated from the equation.

$$D = \left(\frac{C_0 - C}{C_0}\right) \times 100\%$$

where D is the percentage of degradation, C_0 is the concentration of dye where the adsorption–desorption equilibrium is achieved, and C is the concentration at irradiation time t.

The photogenerated radical and hole trapping experiments (scavengers test) with different scavengers were carried out to elucidate the photocatalytic degradation mechanism of MV under similar conditions over AgNdTON. Ammonium oxalate (AO), benzoquinone (BQ), and isopropanol (IPA) were known to scavenge h^+_{VB}, $O_2^{\bullet-}$, and $OH^{\bullet}$, respectively. These scavengers were introduced into the 60 mL aqueous MV dye solution in the presence of AgNdTON catalyst during the photocatalytic reaction and the dye degradation behavior was observed. An additional experiment, terephthalic acid (TA) as a probe, was also carried out to substantiate the formation of $OH^{\bullet}$ radicals during photocatalysis under visible light irradiation as reported earlier [9,28]. The experimental procedure was as follows: 0.05 g of the sample is suspended in 50 mL of a 0.02 M NaOH solution containing 3 Mm of terephthalic acid (TA). The suspension was stirred in the dark for 60 min followed by 180 min of visible light (300 W tungsten lamp) irradiation. Then, 3 mL of the suspension was taken out at 60 -min intervals and filtered, and its fluorescence spectra were recorded using a JASCO FP-8500 spectrofluorometer. It is well known that the photo-generated $OH^{\bullet}$ radicals react with TA to form a 2-hydroxyterephthalic acid (TAOH), which shows a characteristic fluorescence band centered at 426 nm. The increase in the fluorescence intensity is directly proportional to the concentration of photogenerated $OH^{\bullet}$ radicals. The measurement was carried out at the excitation wavelength of 320 nm.

3. Results and discussion

3.1. Characterization studies

The samples were prepared by gel-burning (KNdTO), solid-state (KNdTON), and ion exchange (AgNdTO and AgNdTON) methods. All the compositions were characterized by the powder XRD method. Pristine KNdTO crystallizes in the tetragonal lattice with $I4/mmm$ space group and can intercalate water molecules in the interlayer space

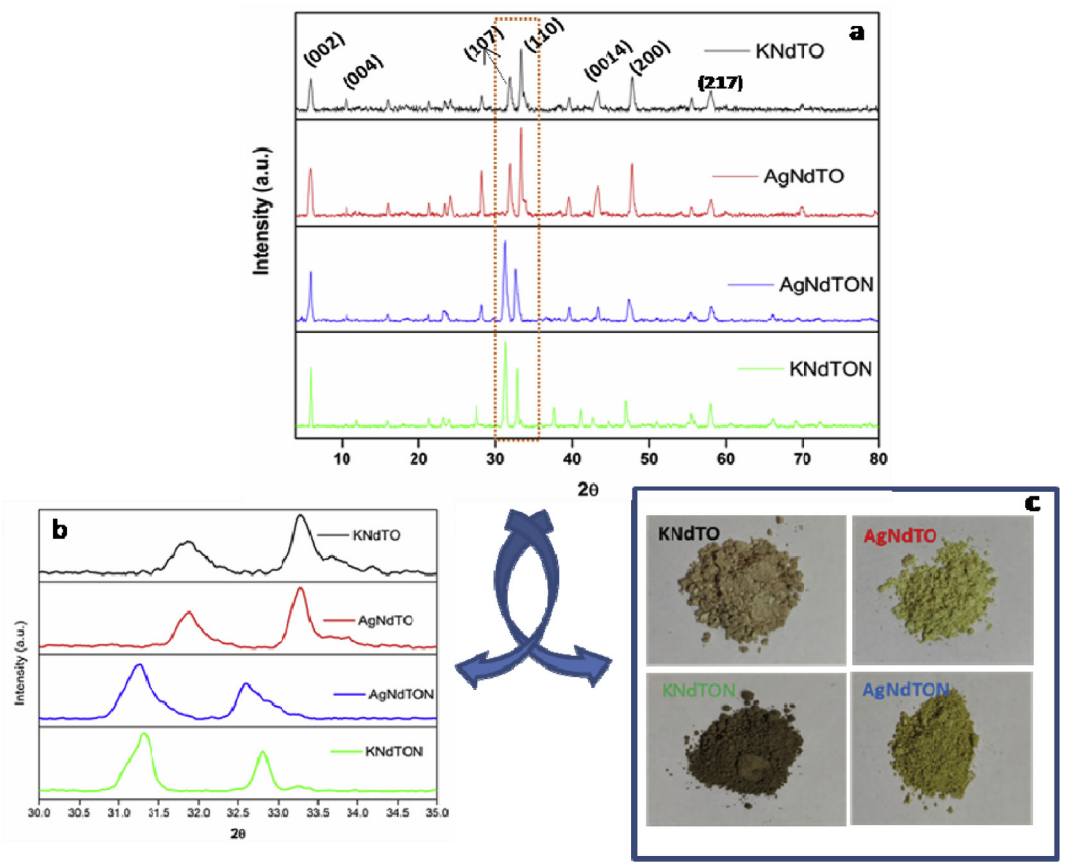

Fig. 2. (a) Powder XRD patterns of KNdTO, KNdTON, AgNdTO, and AgNdTON; (b) enlarged view of selected 2θ (30–35°) region (c); color of respective samples.

when added to water [13–15]. Fig. 2a shows the powder XRD patterns of all the compositions. The powder XRD profile of KNdTO is consistent with reported data [JCPDF No. 87–0479] and free from impurities [14]. The powder XRD profiles of KNdTON, AgNdTO, and AgNdTON are similar to that of KNdTO, which implies that the doping of N^{3-} or Ag^{+} or both ions into a layered perovskite structure did not change the parent lattice. Thus, all the doped samples also crystallized in the tetragonal lattice.

Using the observed *d*-lines of all the samples and POWD software, unit cell parameters were calculated. The unit cell parameters of all the samples are given in Table 1. The doping of N^{3-} or Ag^{+} into a perovskite lattice is endorsed by the observation of shift in the *d*-lines when plotted in an expanded scale (Fig. 2b). The observed shift in the 2θ value confirms the substitution of cation and anions into the KNdTO lattice. The resultant shift in the 2θ value can be ascribed to the difference in the ionic radii of guest and host ions [29,30]. As the ionic radius of doped Ag^{+} (0.74 Å) ion is lower than that of K^{+} (0.97 Å), a decrease in the unit cell parameter and an increase in the 2θ values are expected. However, for AgNdTO, the 2θ values are decreased. This can be explained based on the intercalation property of layered perovskites. During the ion-exchange process, a few water molecules along with Ag^{+} might have entered into the interlayers of lattice leading to an increase in the unit cell parameters and a decrease in 2θ values. The presence of lattice water molecules in doped samples during the ion-exchange reaction is further supported by thermogravimetric (TG) analysis. In the case of KNdTON, as the ionic radius of N^{3-} is higher than that of O^{2-}, an increase in the unit cell parameters and a decrease in the 2θ values are observed. The observed change in the unit cell parameters and shift in 2θ values of AgNdTON are due to the codoping effect (Table 1). The change in the color of the sample due to ion substitution is also displayed in Fig. 2c.

Table 1
Unit cell parameters of KNdTO, KNdTON, AgNdTO, and AgNdTON.

Catalyst	$a = b$ (Å)	c (Å)	Volume (Å^3)
KNdTO	3.844	29.54	436.5
AgNdTO	3.859	29.46	438.8
KNdTON	3.862	29.56	442.2
AgNdTON	3.869	29.84	443.6

TG analysis is carried out to estimate the absorbed or lattice water present in the as-prepared materials during the preparation process and their thermal stability. The TG profiles of all the prepared samples are shown in Fig. 3. The TG profiles of KNdTO and KNdTON are similar to each other. The weight loss observed up to 200 °C for KNdTO (2%) and KNdTON (3%) can be ascribed to the adsorbed water. The TG

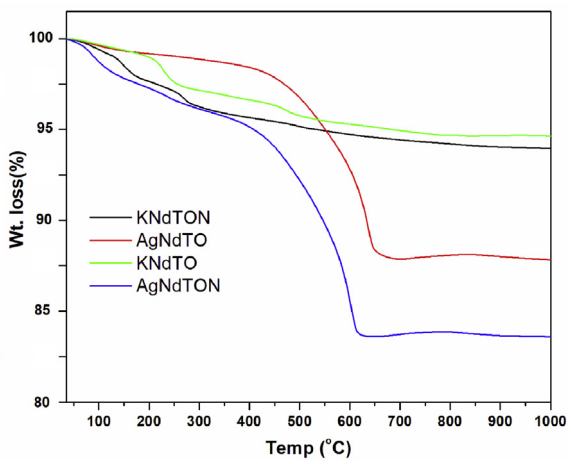

Fig. 3. TG profiles of KNdTO, KNdTON, AgNdTO, and AgNdTON.

profiles of AgNdTO and AgNdTON are comparable. The continuous weight loss observed up to 600 °C for both samples indicates the loss of lattice water, which has entered into interlayers of KNdTO during an ion-exchange reaction carried out in an aqueous medium. The calculated weight loss up to 600 °C for AgNdTO and AgNdTON is ~12% and ~17% respectively.

The surface morphology of KNdTO and AgNdTON is studied by SEM measurements. The SEM images of KNdTO and AgNdTON are presented in Fig. 4. The SEM image of parent KNdTO is characterized by irregular-shaped semi-spherical like objects with considerable agglomeration. The SEM image of doped product AgNdTON is also similar to that of parent KNdTO with relatively less agglomeration, possibly due to the incorporation of guest ion or grinding of the mixture.

To obtain additional information on particle size and morphology of KNdTO and AgNdTON, the TEM and HR–TEM images were recorded. The representative TEM images of the KNdTO and AgNdTON samples are shown in Fig. 5. From these images, it is evident that the morphology of the KNdTO nanoparticles is semi-spherical shape, whereas the AgNdTON sample is composed of spherical-shaped nanoparticles with uniform size. Furthermore, the nanoparticles in the KNdTO sample are more closely aggregated than those in the AgNdTON sample. The particle size histograms determined by measuring ~50–70 nanoparticles with the assumption of spherical-like particles show an average particle diameter of ~15 and 12 nm for KNdTO and AgNdTON, respectively (Fig. 6). This result indicated that the codoping of Ag into the KNdTON lattice results in a slight decrease of particle size.

As shown in Fig. 7a and b, the HR–TEM images of KNdTO and AgNdTON samples clearly show the lattice fringes. The distance between the adjacent lattice fringes is measured as ~1.46 and 1.42 nm, respectively, which agree well with the *d*-spacing value of the (0 0 2) plane of KNdTO. The crystalline nature of both the samples is also studied from SAED (selected area electron diffraction) pattern and the results are displayed in Fig. 7c and d. As shown in this figure, the ring patterns indicate the polycrystalline nature of KNdTO. Furthermore, the diffraction rings are indexed to (0 0 2), (0 0 4), (1 0 7), and (1 1 0) planes, confirming the tetragonal structure of KNdTO, which is consistent with the results of powder XRD.

The doping of cation and anion into KNdTO was further substantiated by EDX, ICP-OES, O–N–H analysis, FT-IR, and UV–vis DRS techniques. The EDX image of KNdTO shows the characteristic peaks corresponding to K, Nd, Ti, and O elements (Fig. 8a). The weight percentages of elements in all the samples obtained from EDX are given in Table 2. The calculated atomic ratio of K:Nd:Ti from EDX data of KNdTO was 1:1:1.5, indicating the molecular formula of KNdTO as $K_2Nd_2Ti_3O_{10}$. The presence of extra peaks corresponding to Ag and N in doped samples supports the doping of Ag^+ and N^{3-} into the parent KNdTO lattice (Fig. 8b). The weight percentage of K, Ag, Nd, and Ti elements present in all the samples was also estimated from ICP-OES. For this purpose, 0.1 g of each sample was dissolved in the acid mixture (5 mL of HNO_3 + 3 mL of HF + 2 mL H_2O_2) using a microwave digestion technique. After complete dissolution of the sample, the samples were analyzed using ICP-OES. The mole ratio of K:Nd:Ti was found to be 1:1:1.5 for the parent material and the mole ratio of Ag:K:Nd:Ti was found to be 0.5:0.5:1:1.5 for the AgNdTO composition. This result shows that 50% of K^+ ions are exchanged by Ag^+ ions. Based on the mole ratio of the materials, the chemical compositions of AgNdTO can be written as $Ag_{0.5}K_{0.5}Nd_2Ti_3O_{10}$. The

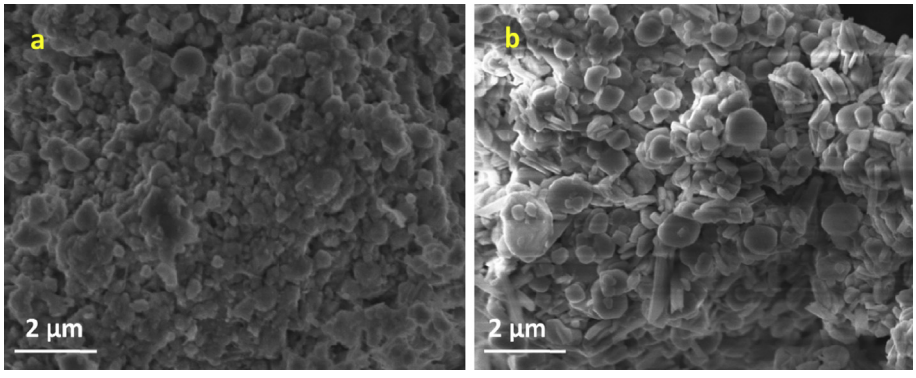

Fig. 4. SEM images of (a) KNdTO and (b) AgNdTON.

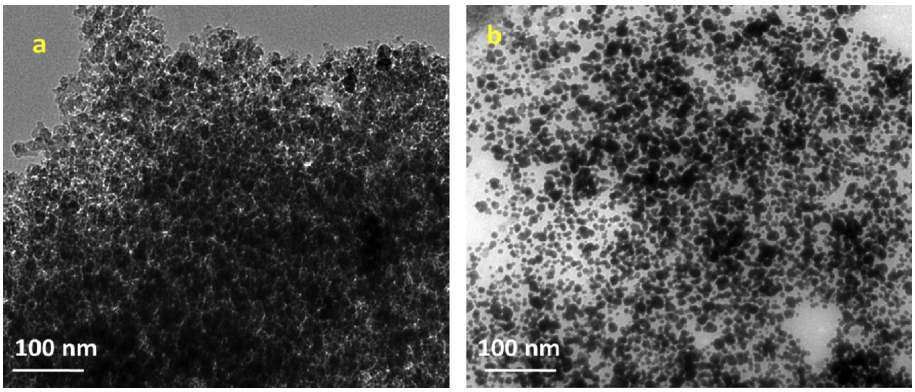

Fig. 5. TEM images of (a) KNdTO and (b) AgNdTON.

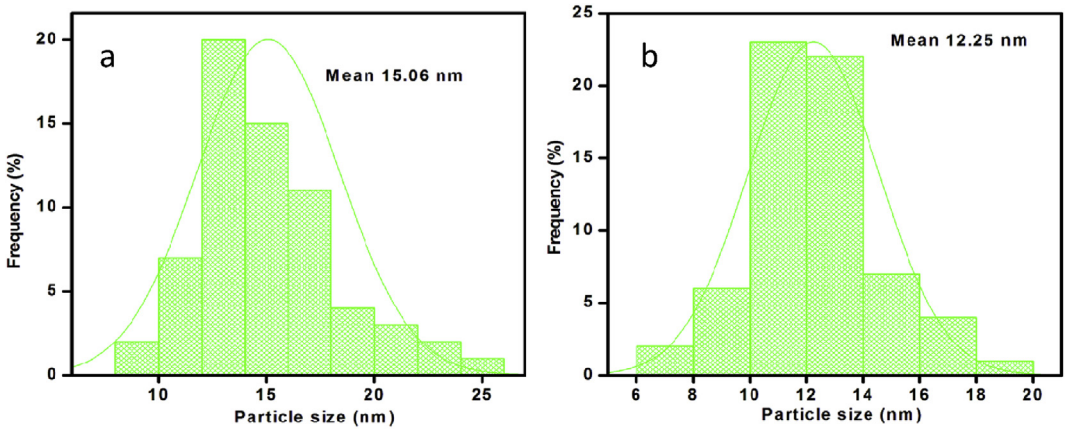

Fig. 6. Particle size histograms of (a) KNdTO and (b) AgNdTON.

mole ratio of K:Nd:Ti was found to be 1:1:1.5 for KNdTON whereas the Ag:K:Nd:Ti ratio was observed to be 0.5:0.5:1:1.5 for AgNdTON compositions. To substantiate the incorporation of N ions into the KNdTO lattice, O–N–H analysis was carried out. The weight percentage of N in KNdTON and AgNdTON was found to be ~2.68 and 2.41, respectively.

The FT-IR spectra of all the compounds were recorded in the range 4000–250 cm^{-1} (Fig. 9). The absorption bands between 350 and 1200 cm^{-1} in all the samples were due to the O–Ti–O stretching vibrational modes [31]. In the case of KNdTON and AgNdTON, new bands in the region 1250–1630 cm^{-1} were observed. As shown in the figure, KNdTON and AgNdTON show three weak bands at ~1260, 1325, and 1645 cm^{-1}. These peaks correspond to the stretching frequencies of N–O/Ag–O species, indicating the doping of N and Ag ions in the KNdTO lattice [32]. The broad peak around at 3100–3400 cm^{-1} corresponds to the N–H stretching vibration and O–H stretching vibration of the adsorbed water molecules [33]. The medium peak at 1370–1420 cm^{-1} corresponds to the asymmetric bending modes of N–H species [34]. The peak noticed in KNdTON and AgNdTON around 2150 cm^{-1} can be assigned to the N=C=O or –N=C=N stretching bonds [26,35]. The vibrational modes observed in the 1300–1700 cm^{-1} region correspond to surface N–H, nitrite, and hyponitrite species [32,36,37].

The UV–vis DRS spectra of all the compositions were obtained to estimate the bandgap energy. Fig. 10a shows the absorbance profiles of KNdTO, AgNdTO, KNdTON, and AgNdTON. It is observed that the absorption edges of the N, Ag, and N/Ag codoped samples shifted remarkably to longer wavelengths compared to that of parent KNdTO. The color change noticed for doped samples also suggests variation in absorption edges (Fig. 2c). The bandgap energy (E_g) of all the compounds was calculated from the Kubelka–Munk plot $((Kh\nu)^{1/2}$ vs hν, where K is the reflectance and $h\nu$ is the photon energy) (Fig. 10b) [38]. The absorption edges of KNdTO, AgNdTO, KNdTON, and AgNdTON observed at ~385, 500, 475, and 485 nm correspond to the bandgap energies of ~3.01, 2.72, 2.85, and 2.51 eV, respectively. The lower bandgap energy of doped samples compared to that of parent KNdTO confirms the doping of Ag^{+} and N^{3-} into its lattice. It is well known that nitrogen enters into the lattice as N^{3-} and occupies the position of oxygen [39]. In the present investigation, N^{3-} is believed to substitute the oxide ion (O^{2-}) in the perovskite lattice leading to vacancy formation. Formation of a vacancy in the

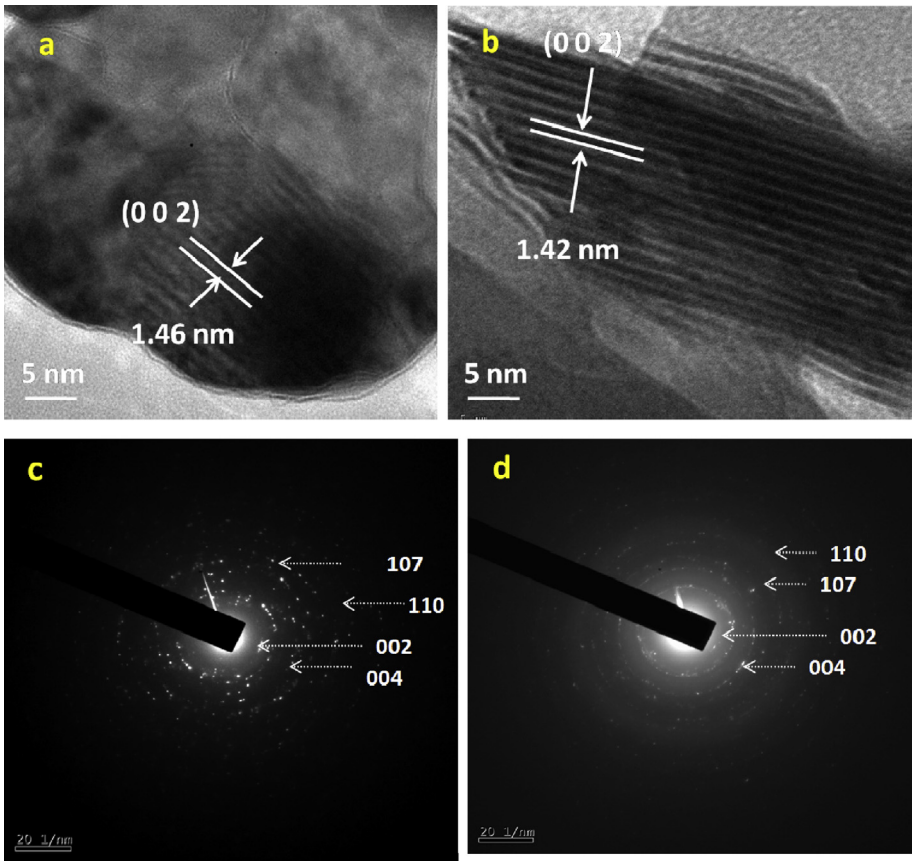

Fig. 7. HR–TEM images (a, b) and SAED patterns (c, d) of KNdTO and AgNdTON.

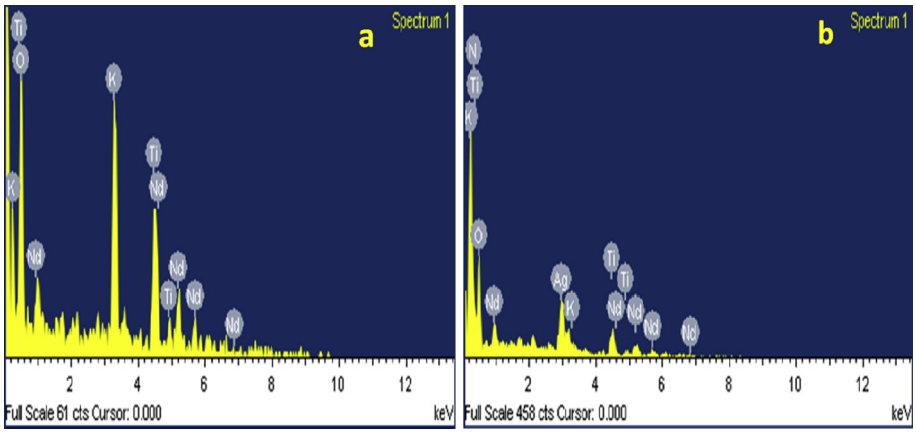

Fig. 8. EDX images of (a) KNdTO and (b) AgNdTON.

lattice may lead to a change in the electronic structure and hence a change in the bandgap energy. A small decrease in E_g (about 0.16 eV) was observed for KNdTON supporting the above hypothesis. The lowering of bandgap energy of AgNdTO, KNdTON, and AgNdTON can be related to the mixing of valence orbital of O 2p with Ag 4d, N 2p to form (Ag 4d + O 2p), (N 2p + O 2p), and (N 2p + O 2p + Ag 4d) hybrid orbitals, respectively. It is well known that in cation/anion doped oxides, the valence orbitals of doped ion mixed with the O 2p orbitals and lifted the band edge of the valence band leading to a reduction in the bandgap energy. Thus, the reduction in the bandgap energy KNdTO can be ascribed to the widening of the valence band, resulting from the hybridization of N 2p and O 2p orbitals [28,29,40].

Table 2
Weight percentages of elements in KNdTO, KNdTON, AgNdTO, and AgNdTON obtained from EDX.

Catalyst	Wt %					
	K	Nd	Ti	O	N	Ag
KNdTO	11.66	43.04	21.42	23.87	–	–
AgNdTO	5.29	39.03	19.42	21.69	–	14.59
KNdTON	11.89	43.87	21.83	19.70	2.68	–
AgNdTON	5.38	39.72	19.76	17.84	2.41	14.85

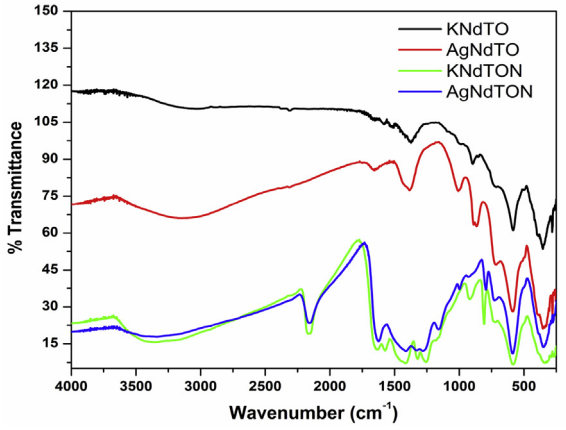

Fig. 9. FT-IR spectra of KNdTO, KNdTON, AgNdTO, and AgNdTON.

Likewise, the upward shifting of valence band because of mixing of Ag 4d and O 2p orbitals led to a decrease in the bandgap energy of AgNdTO and AgNdTON samples. Similar results have been reported in cation and anion-doped semiconductor photocatalysts [26,37,41–43].

3.2. Photocatalytic degradation studies

It is well known that the photocatalytic activity of a material depends on distinct aspects such as its light absorption capability, crystal structure, surface structure, migration of the light-induced electrons and holes, the extent of crystallinity, surface area, and bandgap energy [44]. To validate the photocatalytic degradation studies of the as-prepared perovskites, MB and MV are taken as model pollutants. MB and MV are used extensively in the textile industry as dyeing agents. The degradation behavior of MB and MV in the presence of KNdTO, KNdTON, AgNdTO, and AgNdTON under visible light illumination is shown in Fig. 11. The concentration of both dyes decreased with increase in irradiation time. It is reported that the colored dyes undergo self-degradation (photolysis) to some extent in the presence of light irradiation [45]. The decrease in the concentration of dyes may be due to (i) photolysis or (ii) photodegradation in the presence of catalysts. To validate the process (ii), an additional experiment is carried out under identical experimental conditions without catalyst. It is noticed that MB and MV decomposed to the extent of 22% and 10%, respectively. Thus, the observed decrease in the concentration of dyes is predominantly due to catalysts. The photocatalytic degradation efficiencies of all the catalysts for MB and MV dyes are given in Table 3. It is observed that AgNdTON exhibited higher activity in the degradation of MB and MV compared to that of KNdTO, KNdTON, and AgNdTO, suggesting that N/Ag codoping had an obvious influence on the photocatalytic activity of the KNdTO sample. The decreasing order of the photocatalytic activity of these catalysts against both pollutants is: AgNdTON > AgNdTO > KNdTON > KNdTO.

The higher activity of doped and codoped samples compared to that of the parent compound can be attributed to change in the bandgap energy. The lower bandgap facilitates absorption of more photons and hence formation of a higher number of radicals/holes which facilitate dye degradation. The possible photocatalytic mechanism is as follows [46]:

$$\text{Semiconductor} + h\nu \rightarrow e^-_{CB} + h^+_{VB} \quad \text{i}$$

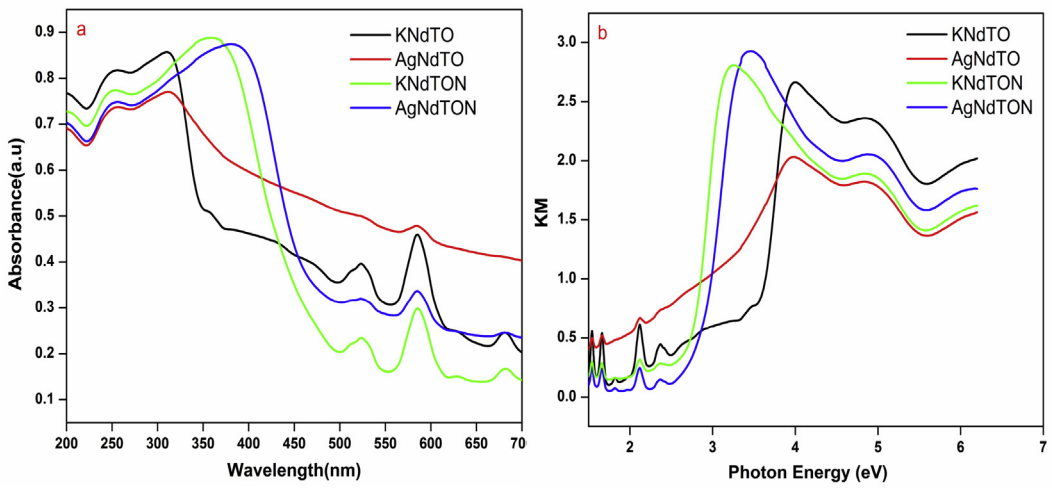

Fig. 10. (a) UV–vis DRS and (b) Kubelka–Munk plots of KNdTO, KNdTON, AgNdTO, and AgNdTON.

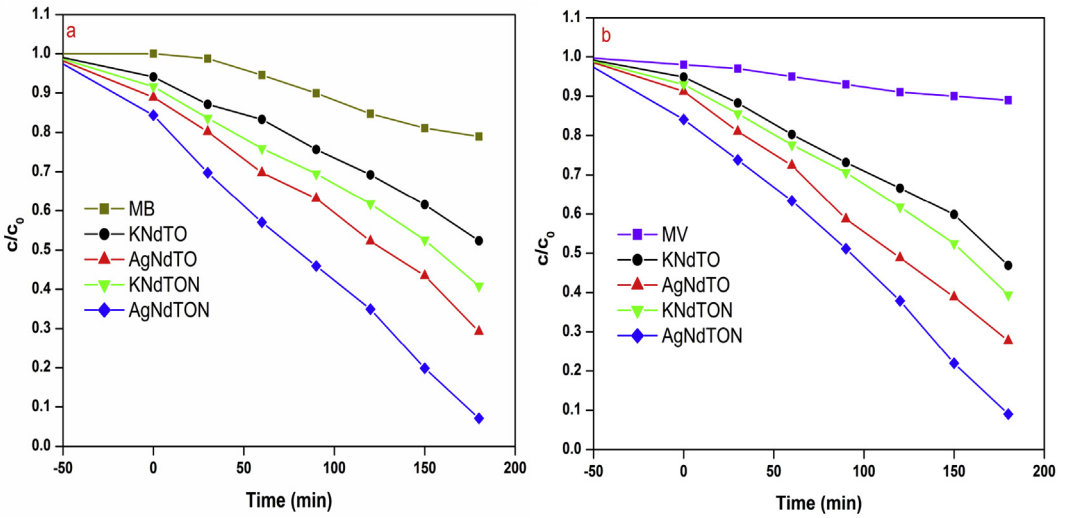

Fig. 11. Photodegradation of (a) MB and (b) MV in the presence and absence of KNdTO, KNdTON, AgNdTO, and AgNdTON under visible-light irradiation.

Table 3
Photocatalytic degradation efficiency of KNdTO, KNdTON, AgNdTO, and AgNdTON for MB and MV dyes.

Catalyst + dye	Degradation (%)	Catalyst + dye	Degradation (%)
MB	22.1	MV	10.2
KNdTO + MB	41.7	KNdTO + MV	45.1
AgNdTO + MB	59.7	AgNdTO + MV	63.5
KNdTON + MB	50.8	KNdTON + MV	53.5
AgNdTON + MB	77.1	AgNdTON + MV	80.1

$$O_2 + e^-_{CB} \rightarrow O_2^{\bullet -} \quad \text{ii}$$

$$(H_2O \rightleftharpoons H^+ + OH^-) + h^+_{VB} \rightarrow H^+ + OH^{\bullet} \quad \text{iii}$$

$$O_2^{\bullet -} + H^+ \rightarrow HO_2^{\bullet} \quad \text{iv}$$

$$2HO_2^{\bullet -} \rightarrow H_2O_2 + O_2 \quad \text{v}$$

$$H_2O_2 + e^- \rightarrow OH^{\bullet} + OH^- \quad \text{vi}$$

$$Dye + OH^{\bullet} \rightarrow dye^{\bullet} + H_2O \quad \text{vii}$$

$$Dye^{\bullet} + h^+ \rightarrow dye^{+\bullet} \rightarrow \text{degradation products}$$

An attempt was made to investigate the role of short-lived photo-induced species that are generated in the degradation process. Generally, species like hydroxyl radicals ($OH^{\bullet}$), superoxide radicals ($O_2^{\bullet -}$), and holes (h^+_{VB}) are responsible for degrading the organic pollutants [47–49]. The photodegradation profiles of MV in the presence of AgNdTON and scavengers are shown in Fig. 12. The photodegradation of MV is considerably suppressed by the addition of BQ ($O_2^{\bullet -}$ scavenger) and AO (h^+_{VB} scavenger). The change in the concentration of MV upon the addition of IPA is less (Table 4). These results imply that $O_2^{\bullet -}$ and h^+_{VB} play a major role in the photodegradation of MV over AgNdTON under visible-light irradiation as compared to that of $OH^{\bullet}$.

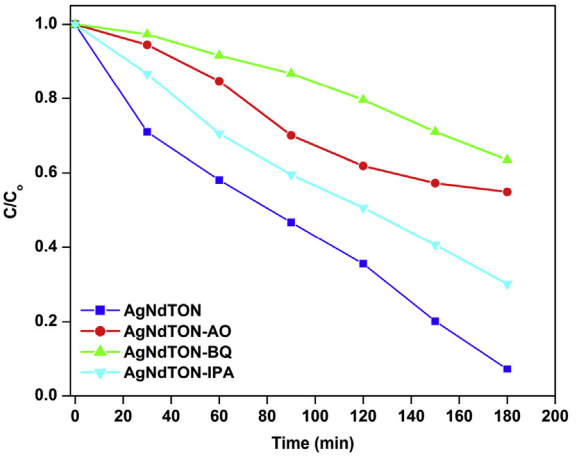

Fig. 12. Photodegradation of MV over AgNdTON in the presence of scavengers.

Table 4
The photocatalytic MV dye degradation percentage in the presence of AgNdTON catalyst and scavengers.

Catalyst + scavenger	Degradation (%)
AgNdTON	81.2
AgNdTON + AO	45.1
AgNdTON + BQ	37.2
AgNdTON + IPA	69.9

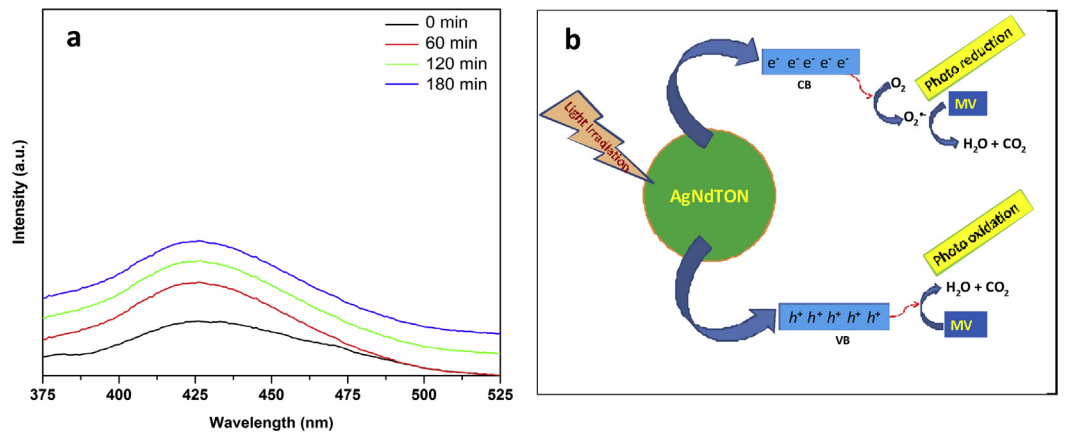

Fig. 13. (a) Fluorescence spectra of visible light irradiated AgNdTON suspension in terephthalic acid solution at room temperature. (b) The proposed mechanism of MV photodegradation over AgNdTON.

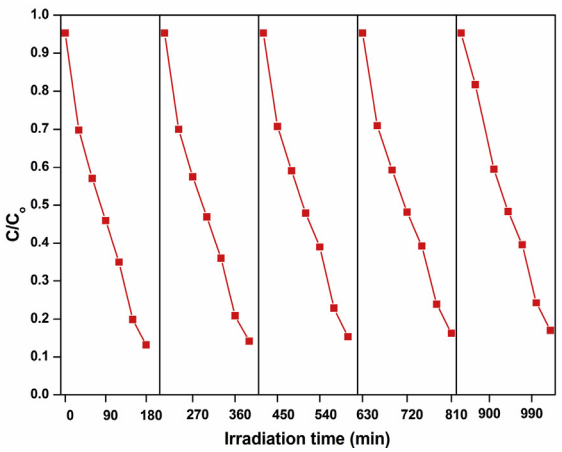

Fig. 14. Cyclic runs in the photodegradation of MV in the presence of AgNdTON.

The minor role of OH• in the photodegradation of MV is further supported by a fluorescence technique using terephthalic acid (TA) as a probe [46]. It is documented that OH• reacts with TA and forms 2-hydroxyterephthalic acid (TAOH), which gives a characteristic fluorescence signal at 426 nm at the excitation wavelength of 320 nm. As shown in Fig. 13a, the small increase in the fluorescence signal at regular time intervals for the visible light irradiated TA in the presence of AgNdTO catalyst at 426 nm indicates less number of OH• radicals generated during the photocatalytic reaction. This result endorses the minor role of OH• in the photodegradation of MV in the presence of AgNdTON catalyst. Based on these experimental results, a plausible mechanism for the photocatalytic MV degradation over AgNdTON catalyst under visible light irradiation is shown in Fig. 13b.

The chemical stability and reusability of a catalyst are essential for commercial application of catalysts. In the present investigation, the stability and reusability of AgNdTON catalyst are tested with recycling experiments. The catalyst (AgNdTON) used in the first cycle is separated at the end of the experiment, dried, and used in the second cycle with a fresh dye solution. The procedure is repeated up to five cycles under identical experimental conditions and the change in the concentration of dye with time is plotted (Fig. 14). Up to five successive cycles, the percentage of degradation is almost the same indicating that the catalyst is chemically stable and can be used at least up to five cycles. The marginal decrease in the percentage of dye degradation in the fifth cycle is probably due to the loss of some catalyst during the recovery process (Table 5).

Table 5
Efficiency of AgNdTON catalyst over MV dye up to 5 cycles.

Catalyst	Degradation (%)				
	First cycle	Second cycle	Third cycle	Fourth cycle	Fifth cycle
AgNdTON	82.2	81.3	80.5	79.7	78.7

4. Conclusions

In this work, N-doped, Ag-doped, and N/Ag-codoped KNdTO are successfully synthesized and applied as photocatalysts for the degradation of MB and MV under visible light irradiation. It is observed that doping and codoping of ions considerably enhance the photocatalytic activity of parent KNdTO. The XRD patterns confirm that parent KNdTO, doped and codoped KNdTO, crystallizes in the tetragonal lattice. The SEM images validate that the parent KNdTO and N/Ag-codoped KNdTO catalysts possessed nanosized semi-spherical and spherical particles, respectively. The AgNdTON catalyst exhibited higher visible light induced degradation of MB and MV compared to N-doped KNdTO, Ag-doped KNdTO, and KNdTO. The higher photocatalytic activity of AgNdTON is ascribed to its higher visible light absorption and narrowing of bandgap energy. The scavenging studies revealed that h^{+}_{VB} and $O_2^{\bullet-}$ are the main active species involved in the MV dye degradation

reaction. Besides, AgNdTON is chemically stable up to five recycling experiments. Thus, AgNdTON catalyst can be exploited further in photocatalytic applications.

Acknowledgements

The Science and Engineering Research Board (SERB) (Grant No. EMR/2016/001533), Department of Science and Technology (DST), India, is acknowledged for its financial support. MV thanks UGC, New Delhi for the award of BSR fellowship [F.18–1/2011(BSR)].

References

[1] I.A. Rodionov, I.A. Zvereva, Russ. Chem. Rev. 85 (2016) 248–279.
[2] H.K. Hakki, S. Allahyari, N. Rahemi, M. Tasbihi, C. R. Chimie 22 (2019) 393–405.
[3] A. Indra, P.W. Menezes, M. Driess, C. R. Chimie 21 (2018) 909–915.
[4] M.R. Hoffmann, S.T. Martin, W. Choi, D.W. Bahnemann, Chem. Rev. 95 (1995) 69–96.
[5] X. Chen, S. Shen, L. Guo, S.S. Mao, Chem. Rev. 110 (2010) 6503–6570.
[6] F.E. Osterloh, Chem. Mater. 20 (2008) 35–54.
[7] A. Kudo, Y. Miseki, Chem. Soc. Rev. 38 (2009) 253–278.
[8] X. Xu, Y. Zhong, Z. Shao, Trends Chem. 4 (2019) 410–424.
[9] G. Amow, S.J. Skinner, J. Solid State Electrochem. 10 (2006) 538–546.
[10] O. Silyukov, M. Chislov, A. Burovikhina, T. Utkina, I. Zvereva, J. Therm. Anal. Calorim. 110 (2012) 187–192.
[11] J. Yu, J. Sunarso, Y. Zhu, X. Xu, R. Ran, W. Zhou, Z. Shao, Chem. Eur J. 22 (2016) 2719–2727.
[12] R.E. Schaak, T.E. Mallouk, Chem. Mater. 14 (2002) 1455–1471.
[13] J. Gopalakrishnan, V. Bhat, Inorg. Chem. 26 (1987) 4299–4301.
[14] M. Richard, L. Brohan, M. Tournoux, J. Solid State Chem. 112 (1994) 345–354.
[15] Y.S. Hong, C.H. Han, K. Kim, J. Solid State Chem. 158 (2001) 290–298.
[16] L.L. Zhang, W. Zhang, J. Zhu, L.D. Lu, X. Yang, X. Wang, J. Solid State Chem. 178 (2005) 761–768.
[17] L.L. Zhang, M. Ji, H. Wang, L.D. Lu, X. Yang, X. Wang, Mater. Lett. 60 (2006) 3100–3103.
[18] I.A. Rodionov, O.I. Silyukov, T.D. Utkina, M.V. Chislov, Y.P. Sokolova, I.A. Zvereva, Russ. J. Gen. Chem. 82 (2012) 1191–1196.
[19] T. Utkina, M. Chislov, O. Silyukov, A. Burovikhina, I.A. Zvereva, J. Therm. Anal. Calorim. 125 (2016) 281–287.
[20] T. Utkina, M. Chislov, M. Myshenkov, I. Rodionov, I. Zvereva, J. Therm. Anal. Calorim. 134 (2018) 323–331.
[21] N.M. Hagh, G.G. Amatucci, J. Power Sources 256 (2014) 457–469.
[22] A. Luque, A. Marti, Phys. Rev. Lett. 78 (1997) 5014–5017.
[23] X. Xu, C. Su, W. Zhou, Y. Zhu, Y. Chen, Z. Shao, Adv. Sci. 3 (2016) 1500187–1500192.
[24] W. Zhu, X. Qiu, V. Iancu, X.-Q. Chen, H. Pan, W. Wang, N.M. Dimitrijevic, T. Rajh, H.M. Meyer, M.P. Paranthaman, G.M. Stocks, H.H. Weitering, B. Gu, G. Eres, Z. Zhang, Phys. Rev. Lett. 103 (2009) 226401–226404.
[25] X. Sun, Y. Mi, F. Jiao, X. Xu, ACS Catal. 8 (2018) 3209–3221.
[26] V.K. Govind, S. Uma, J. Hazard Mater. 189 (2011) 502–508.
[27] V. Jeyalakshmi, R. Mahalakshmy, K. Ramesh, P.V.C. Rao, N.V. Choudary, G.S. Ganesh, K. Thirunavukkarasu, K.R. Krishnamurthy, B. Viswanathan, RSC Adv. 5 (2015) 5958–5966.
[28] K. Ramaswamy, V. Radha, K. Sreenu, G. Ravi, N.R. Munirathnam, M. Vithal, Mater. Res. Express 3 (2016) 115902.
[29] S. Uma, J. Singh, V. Thakral, Inorg. Chem. 48 (2009) 11624–11630.
[30] G. Ravi, N.K. Veldurthi, P. Suresh, V. Radha, P. Someshwar, J.R. Reddy, M. Vithal, Photochem. Photobiol. 89 (2013) 824–831.
[31] T.C. Jagadale, S.P. Takale, R.S. Sonawane, H.M. Joshi, S.I. Patil, B.B. Kale, S.B. Ogale, J. Phys. Chem. C 112 (2008) 14595–14602.
[32] F. Zou, Z. Jiang, X. Qin, Y. Zhao, L. Jiang, J. Zhi, T. Xiao, P.P. Edwards, Chem. Commun. 48 (2012) 8514–8516.
[33] M.S. Azami, W.I. Nawawi, A.H. Jawad, M.A.M. Ishak, K. Ismail, Sains Malays. 46 (2017) 1309–1316.
[34] B. Tian, Y. Qian, B. Hu, J. Sun, Z. Du, J. Mater. Res. 27 (2012) 2408–2416.
[35] D.J.V. Pulsipher, I.T. Martin, E.R. Fisher, ACS Appl. Mater. Interfaces 2 (2010) 1743–1753.
[36] S. Sakthivel, M. Janczarek, H. Kisch, J. Phys. Chem. B 108 (2004) 19384–19387.
[37] V. Radha, K. Ramaswamy, G. Ravi, N.R. Munirathnam, M. Vithal, Z. Anorg. Allg. Chem. 641 (2015) 935–940.
[38] P. Venkataswamy, D. Jampaiah, A.E. Kandjani, Y.M. Sabri, B.M. Reddy, M. Vithal, Res. Chem. Intermed. 44 (2018) 2523–2543.
[39] Y. Liu, W. Wang, X. Xu, J.P.M. Veder, Z. Shao, J. Mater. Chem. A7 (2019) 7280–7300.
[40] G. Ravi, S. Mansouri, P. Suresh, M. Vithal, Indian J. Chem. 54A (2015) 20–26.
[41] H. Tong, S. Ouyang, Y. Bi, N. Umezawa, M. Oshikiri, J. Ye, Adv. Mater. 24 (2012) 229–251.
[42] M. Li, J. Zhang, W. Dang, S.K. Cushing, D. Guo, N. Wu, P. Yin, Phys. Chem. Chem. Phys. 15 (2013) 16220–16226.
[43] H. Zhang, G. Chen, Y. Li, Y. Teng, Int. J. Hydrogen Energy 35 (2010) 2713–2716.
[44] J. Tang, Z. Zou, J. Ye, Chem. Mater. 16 (2004) 1644–1649.
[45] D. Chatterjee, A. Mahata, J. Photochem. Photobio. A Chem. 153 (2002) 199–204.
[46] T. Hirakawa, Y. Nosaka, Langmuir 18 (2002) 3247–3254.
[47] S. Kumar, T. Surendar, A. Baruah, V. Shanker, J. Mater. Chem. 1 (2013) 5333–5340.
[48] N. Zhang, Y. Zhang, M.-Q. Yang, Z.-R. Tang, Y.-J. Xu, J. Catal. 299 (2013) 210–221.
[49] Y.-S. Xu, W.-D. Zhang, Dalton Trans. 42 (2013) 1094–1101.